PAPER

Microwave-assisted hydrothermal synthesis of graphene based Au–TiO$_2$ photocatalysts for efficient visible-light hydrogen production

Ying Wang,[a] Jiaguo Yu,*[a] Wei Xiao*[b] and Qin Li[a]

The construction and application of visible-light-driven photocatalysts falls in the central focus for the efficient utilization of renewable solar energy, which provides unprecedented opportunities for addressing the increasing concerns on energy and environmental sustainability. Herein, graphene based Au–TiO$_2$ photocatalysts were fabricated by a simple, one-step microwave-assisted hydrothermal method, using Degussa P25 TiO$_2$ powder (P25), graphene oxide and HAuCl$_4$ aqueous solution as the raw materials. The effects of graphene introduction and gold loading on the photocatalytic hydrogen production rates of the as-prepared samples in a methanolic aqueous solution were investigated. The results indicated that Au–TiO$_2$–graphene composite had a significantly increased visible light absorption and enhanced photocatalytic H$_2$-production activity compared to the Au–TiO$_2$ composite. In comparison, the pure TiO$_2$, graphene–TiO$_2$ and graphene–Au had no appreciable visible-light-driven H$_2$ production. The enhanced photocatalytic H$_2$-production activity of the Au–TiO$_2$–graphene composite is ascribed to (1) the load of the Au nanoparticles which broadens the visible light response of TiO$_2$ due to the surface plasmon resonance (SPR) effect, and (2) the introduction of graphene, which functions as rapid electron transfer units, facilitating the space separation of photoelectrons and hole pairs. The proposed H$_2$-production activity enhancement mechanism was further confirmed by the transient photocurrent response and electrochemical impedance spectroscopy (EIS) experiments.

1. Introduction

With the emergence of energy crises and environmental problems resulting from the combustion of depleting fossil fuels, storable, clean, and environmentally friendly hydrogen energy is well recognized as an ideal alternative to fossil fuels. As a sustainable approach for hydrogen production, photocatalytic water splitting using semiconductor photocatalysts is a promising and attractive way for hydrogen generation.[1,2] Titanium dioxide (TiO$_2$) has been extensively investigated as a state-of-the-art semiconductor photocatalyst, due to its excellent properties such as non-toxicity, low cost, long-term stability against photocorrosion and chemical corrosion, and strong oxidizing and reducing power.[3] However, the hydrogen production efficiency of intrinsic TiO$_2$ remains quite limited, mainly due to the rapid recombination rate of the photogenerated electron–hole pairs within the TiO$_2$ particles and the limited UV-light response.[4,5]

Correspondingly, many methods have been proposed to enhance the photocatalytic activity of TiO$_2$, such as metal loading,[6] non-metal doping,[7,8] dye sensitization,[9] and the addition of sacrificial reagents[10,11] (electron donors or hole scavengers). By depositing noble metals, such as Pt[12] and Pd[13] onto the surface of TiO$_2$, an enhanced UV-light photocatalytic capability of TiO$_2$ was achieved, due to the electron-trapping effect of the deposited noble metals, facilitating the space separation of photo-induced charge carriers, in which utilization of the full solar spectrum remained unsatisfactory. Actually, UV radiation only accounts for 4% of the solar spectrum. In this sense, photocatalysts capable of utilizing solar irradiation more efficiently are more promising.

Recently, plasmonic nanostructures of metals like Au,[14,15] Ag[16] and Cu[17] have generated enormous attention, because they can strongly interact with irradiation in the visible and infrared regions, due to their extraordinary localized surface plasmon resonance (SPR). Surface plasmon resonances are derived from the collective oscillations of the electrons close to the surface plasmonic nanostructures by the electric field of the incident light. Nanostructures that have strong and broad absorption bands in the visible light region can be designed by means of manipulating the composition, shape, and size of the plasmonic nanoparticles. In addition, owing to the high specific surface area and superior electron mobility, graphene,

[a]State Key Laboratory of Advanced Technology for Material Synthesis and processing, Wuhan University of Technology, Wuhan, 430070, P. R. China. E-mail: jiaguoyu@yahoo.com; Fax: +86-27-87879468; Tel: +86-27-87871029

[b]Department of Environmental Engineering, School of Resource & Environmental Sciences, Wuhan University, Wuhan, 430072, P. R. China. E-mail: gabrielxiao@whu.edu.cn; Fax: +86-27-68775799; Tel: +86-27-68775799

functioning as an ideal sink for photogenerated electrons has been considered to be a high-performance support for photocatalysts and an efficient co-catalyst for hydrogen production.[18,19] For instance, Lightcap et al.[20] verified that graphene can store and shuttle electrons, working as semiconductor photocatalyst mats for effective electron transfer. Xiang et al.[21] reported that graphene–TiO$_2$ nanosheet composites, synthesized under microwave-assisted hydrothermal conditions, showed an enhanced photocatalytic hydrogen production activity.

Although photocatalytic hydrogen production from splitting water over metal–TiO$_2$ (ref. 4) and graphene–TiO$_2$ (ref. 21) composites is well-documented, Au–TiO$_2$–graphene composites for hydrogen production remain less explored. Herein, we report the one-step, microwave-assisted hydrothermal synthesis and photocatalytic properties of Au–TiO$_2$–graphene ternary composites. The as-obtained photocatalyst shows an enhanced visible-light-driven photocatalytic hydrogen production activity, due to the SPR effect of Au and the superior electron-transfer properties of graphene.

2. Experimental

2.1. Preparation

The Au–TiO$_2$–graphene composites were prepared by a simple microwave-hydrothermal method using ethanol–water as the solvent. Graphene oxide (GO) was synthesized from natural graphite powder (>99.8%, Alfa Aesar) by a modified Hummers' method.[22] In a typical synthesis of the composite, 0.2 mg of the prepared GO was dispersed in a mixed solution of distilled H$_2$O (20 mL) and ethanol (10 mL) by ultrasonic treatment for 1 h, and then 0.2 g of the TiO$_2$ (P25) was added to the obtained GO and TiO$_2$ mixed solution and stirred for another 5 min. A varying amount of 0.01 mol L^{-1} HAuCl$_4$ solution was then added to the mixed solution and stirred for another 1 h to obtain the homogeneous solution. The weight ratios of Au to the TiO$_2$–GO composite were controlled to be 0, 0.05%, 0.1%, 0.25%, and 0.5%, and the obtained samples were labeled as PG, PGA05, PGA10, PGA25 and PGA50, respectively. Next, the homogeneous solution was transferred into a 70 mL Teflon-lined autoclave, which was then placed in a microwave-hydrothermal synthesis system (MDS-6, Sineo, Shanghai, China) and maintained at 180 °C for 1 h, during which the simultaneous reduction of GO and deposition of Au nanoparticles on the TiO$_2$ occurred. After the hydrothermal reaction, the resulting composite was collected and washed with distilled water, followed by rinsing in ethanol, and then dried in an oven at 80 °C, for 6 h, in the air. For comparison, pure TiO$_2$ (labeled as P), Au–TiO$_2$ nanoparticle composites (with the content of gold, 0.25 wt%, labeled as PA25) and graphene–Au composite (the weight ratio of graphene–Au = 28.6, labeled as GA) were also prepared via the microwave-hydrothermal route, under the same conditions.

2.2. Characterization

Transmission electron microscopy (TEM) analyses were conducted with a JEM-2100F electron microscope (JEOL, Japan), using a 200 kV accelerating voltage. Powder X-ray diffraction (XRD) patterns were obtained on a D/Max-RB X-ray diffractometer (Rigaku, Japan) with Cu Kα radiation (λ = 0.15418 nm) at a scan rate (2θ) of 0.05° s^{-1}. The accelerating voltage and the applied current were 40 kV and 80 mA, respectively. The Brunauer–Emmett–Teller specific surface areas (S_{BET}) and the porosity of the samples were evaluated on the basis of nitrogen adsorption isotherms, measured at −196 °C, using a Micromeritics ASAP 2020 gas adsorption apparatus (USA). All the samples were degassed at 180 °C before the nitrogen adsorption measurements. The BET surface area was determined using the adsorption data in the relative pressure (P/P_0) range of 0.05–0.3. The desorption data were used to determine the pore-size distribution via the Barrett–Joyner–Halender (BJH) method.[23] The nitrogen adsorption volume at the relative pressure (P/P_0) of 0.99 was used to determine the single-point pore volume and the average pore size. Raman spectra were recorded at room temperature using a micro-Raman spectrometer (Renishaw In Via) in the backscattering geometry with a 514.5 nm Ar$^+$ laser as the excitation source. X-Ray photoelectron spectroscopy (XPS) measurements were performed by using an ultrahigh vacuum ESCALAB250xi electron spectrometer equipped with a multi-channel detector. The spectra were excited using X-ray monochromatisation radiation (operated at 200 W). All the binding energies were referenced to the adventitious C1s peak at 284.8 eV. UV-visible absorbance spectra were obtained for the dry-pressed disk samples with a UV-visible spectrophotometer (UV-2550, Shimadzu, Japan). BaSO$_4$ was used as a reflectance standard in the UV-visible diffuse reflectance experiment.

2.3. Photocatalytic H$_2$-production activity

The photocatalytic H$_2$-production experiments were performed in a 100 mL Pyrex flask at ambient temperature and atmospheric pressure, with the flask being sealed with a silicone rubber septum. Four low-power 420 nm-LEDs (3 W) (Shenzhen LAMPLIC Science Co. Ltd., China), which were positioned ca. 1 cm away from the reactor in four different directions, were used as the light sources to trigger the photocatalytic reaction. The focused intensity and areas on the flask for each 420 nm-LED were ca. 80.0 mW cm^{-2} and 1 cm^2, respectively. In a typical photocatalytic experiment, 50 mg of the Au–TiO$_2$–graphene photocatalyst was suspended in 80 mL of a mixed solution of methanol (20 mL) and water (60 mL). Prior to irradiation, the suspension of the catalyst was dispersed in an ultrasonic bath for 5 min and then nitrogen was bubbled through the reactor, for 30 min, to completely remove the dissolved oxygen and ensure that the reactor was in an anaerobic condition. A continuous magnetic stirring was applied at the bottom of the reactor in order to keep the photocatalyst particles in suspension during the whole experiment. 0.4 mL gas was intermittently sampled through the septum, and the hydrogen was analyzed by a gas chromatograph (GC-14C, Shimadzu, Japan, TCD, nitrogen as a carrier gas and 5 Å molecular sieve column).

All the glassware was carefully rinsed with distilled water, prior to use. The quantum efficiency (QE) was measured and calculated according to eqn (1):

$$QE[\%] = \frac{\text{number of reacted electrons}}{\text{number of incident photons}} \times 100$$

$$= \frac{\text{number of evolved } H_2 \text{ molecules} \times 2}{\text{number of incident photons}} \times 100 \qquad (1)$$

2.4. Photoelectrochemical measurements

The photocurrents and electrochemical impedance spectroscopy (EIS) were measured using an electrochemical analyzer (CHI660C Instruments) in a standard three-electrode system, in which a Pt wire and Ag/AgCl (saturating KCl) functioned as the counter electrode and reference electrode, respectively. A 3 W 420 nm-LED lamp was utilized as the light source. A 0.5 M Na_2SO_4 aqueous solution was used as the electrolyte. For the working electrodes, 0.2 g of the photocatalyst (samples P, PG, PA25 and PGA25) was ground with 0.06 g polyethylene glycol (PEG, molecular weight 20 000) and 1.0 mL ethanol to make a slurry. Afterward, the slurry was coated onto a 2 cm × 1.5 cm F-doped SnO_2-coated glass (FTO glass) electrode by the doctor blade method, with an active area of *ca.* 1 cm². Upon drying in an oven, the electrodes were calcined at 450 °C for 30 min. All the electrodes used had a similar thickness (12–15 μm). The transient photocurrent curves were measured under an applied bias of 0.5 V and the EIS measurements were carried out by applying the bias of the open circuit voltage (VOC) and recorded over a frequency range of 0.1×10^5 Hz with an ac amplitude of 10 mV.

3. Results and discussion

3.1. Phase structures and morphology

XRD was used to investigate the changes of the phase structures and crystallite size of the as-prepared samples. Fig. 1 presents the comparison of the XRD patterns of the samples (P, PG,
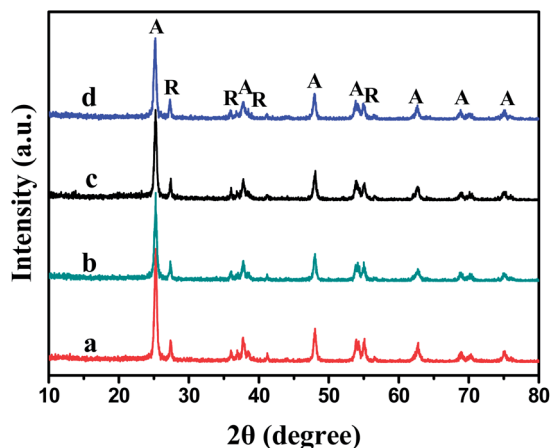

Fig. 1 XRD patterns of the samples P (a), PG (b), PA25 (c) and PGA25 (d).

PGA25 and PA25). As can be seen from this figure, the anatase [JCPDS no. 21-1272] and rutile [JCPDS no. 21-1276] phases of TiO_2 are observed for the pure TiO_2 (sample P), graphene–TiO_2 (sample PG), Au–TiO_2 (sample PA25) and Au–TiO_2–graphene (samples PGA25). No characteristic diffraction peaks of Au are observed for samples PA25 and PGA25, because of its low loading content. Further observation indicates that there is no obvious change observed in the diffraction peak position of the anatase and rutile TiO_2, suggesting that the Au nanoparticles do not incorporate into the lattice of TiO_2. Notably, no characteristic diffraction peaks for the carbon species are observed in the patterns, because of the low amount and relatively low diffraction intensity of graphene.[21] The average crystallite sizes of anatase and rutile were calculated using Scherrer's equation, from the main diffraction peak of anatase (101) and rutile (110), respectively. As listed in Table 1, all the samples have almost the same crystallite size (*ca.* 21 nm for anatase and 30 nm for rutile), implying that the introduction of Au into TiO_2 has no obvious influence on its crystallite size and morphology, which confirms that the Au is highly dispersed on the surface of the TiO_2.[24]

TEM was used to further observe the morphology and microstructures of the as-prepared samples. Fig. 2a presents a TEM image of the Au–TiO_2–graphene (sample PGA25), clearly indicating that Au nanoparticles (NPs) with size of 12–15 nm are uniformly deposited on the surface of the TiO_2 nanoparticles, in which the thin, two-dimensional graphene sheet serves as the support. The HRTEM image in Fig. 2b shows the lattice fringes of the Au NPs, with spacings of 0.23 nm, 0.20 nm, 0.15 nm and 0.12 nm corresponding to the (111), (200), (220) and (311) lattice planes, respectively, of the Au NPs. This result indicates that the $HAuCl_4$ precursor was successfully converted to metallic Au NPs, with a face-centered cubic (fcc) structure, during the reduction process.[25] In addition, another four kinds of lattice fringes around the Au NPs, with *d* spacings of about 0.35, 0.24, 0.13 and 0.32 nm were observed by HRTEM, which can be indexed as the (101), (103) and (301) planes of the anatase TiO_2 and (110) plane of rutile TiO_2, respectively. Thus, a close contact and good incorporation among the Au, TiO_2 and graphene components, achieved by the hydrothermal processing is believed to favor the transfer of photogenerated electrons between the Au NPs, TiO_2 and graphene sheets, thus enhancing the charge separation and photocatalytic efficiency.

3.2. BET surface areas and pore structures

Broadly speaking, photocatalysts with high specific surface areas and large pore volumes are helpful for the enhancement of photocatalytic performance, owing to enhanced adsorption of reactant molecules, fast transportation of reactant molecules and products, and enhanced harvesting of light.[26–29] Fig. 3 shows the nitrogen adsorption–desorption isotherms and the corresponding pore-size distribution curves (inset) of the P, PG, PA25 and PGA25 samples. It can be seen that all the samples have isotherms of type IV, from the Brunauer–Deming–Deming–Teller (BDDT) classification, indicating the presence of mesopores (2–50 nm).[23,27] The isotherms exhibit H3 hysteresis loops at a high relative pressure range of 0.8 to 1.0, indicating

Table 1 Effects of graphene and Au introduction on physicochemical properties and QE of the prepared samples

Samples	Graphene (wt%)	Gold (wt%)	ACS^a (nm)	S_{BET} (m^2 g^{-1})	PV^b (cm^3 g^{-1})	Average pore size (nm)	QE (%)
P	0	0	21.7 (A), 30.0 (R)	48.2	0.10	7.0	0
PG	0.10	0	21.0 (A), 30.9 (R)	49.3	0.10	8.0	0
PGA25	0.10	0.25	20.8 (A), 30.7 (R)	50.1	0.13	10.0	4.1
PA25	0	0.25	20.5 (A), 30.0 (R)	57.5	0.14	9.5	2.4

^{a} A and R denote anatase and rutile, respectively. ACS: Average crystallite size. ^{b} PV: Pore volume.
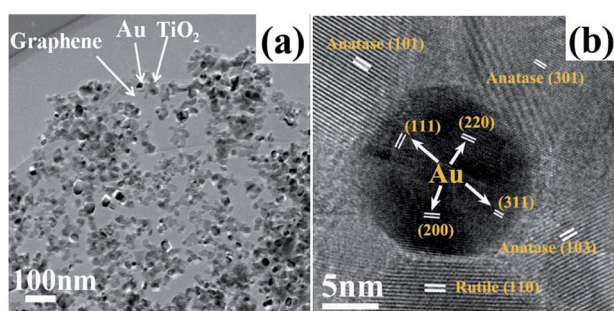

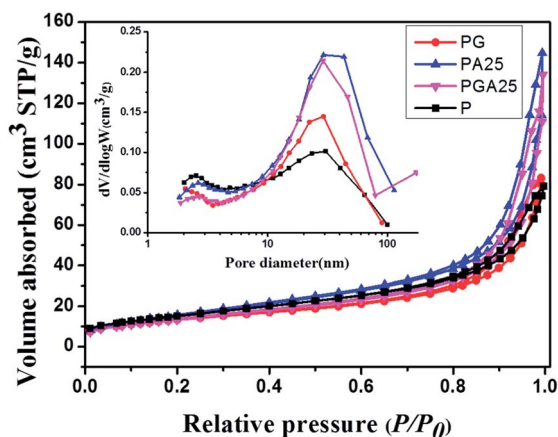**Fig. 2** TEM (a) and HRTEM (b) images of the PGA25 sample.

Fig. 3 Nitrogen adsorption–desorption isotherms and the corresponding pore-size distribution curves (inset) of the P, PG, PA25 and PGA25 samples.

the presence of slit-like pores. There is a high absorption at a high relative pressure (P/P_0) range (approaching 1.0), implying the formation of large mesopores and macropores.[4,23,27] A further observation shows that the isotherms of sample PGA25 shift up, compared to samples P and PG, suggesting a higher surface area of the sample PGA25. The pore-size distribution curves (see inset of Fig. 3), calculated from the desorption branch of the nitrogen isotherms by the BJH method, show a wide range, from 2 to over 100 nm, with a peak pore diameter of about 30 nm for the samples P, PG, PA25 and PGA25, indicating the existence of mesopores and macropores, due to the entangling of graphene sheets and aggregation amongst the TiO$_2$ NPs, Au NPs and graphene nanosheets.[23] Table 1 shows

that the Au–TiO$_2$–graphene composite samples have larger specific surface areas than the pure TiO$_2$ and graphene–TiO$_2$. This is due to the presence of graphene in the composites, which has an extremely high surface area.[21] Moreover, the deposition of Au nanoparticles causes the formation of more aggregation of TiO$_2$ crystallites. Such aggregated porous structures might provide efficient transport pathways for reactant and product molecules and therefore are useful in the photocatalytic process.[28,29] However, the BET surface area and pore volume of sample PGA25 decrease, compared with the PA sample, which is due to the fact that the graphene coating on the surface of TiO$_2$ has blocked some mesopores and micropores.[29]

3.3. UV-vis diffuse reflection spectra

The UV-vis diffuse reflectance spectra of the P, PG, PA25 and PGA25 samples are shown in Fig. 4. All the samples studied display a typical absorption, with an intense transition at ∼410 nm, indicating a band gap of 3.0 eV. Such a band gap value corresponds to the intrinsic band gap absorption of rutile TiO$_2$.[30] With the introduction of graphene, the graphene–TiO$_2$ composites (sample PG) display the same absorption edge as pure TiO$_2$ (sample P, Fig. 4a), implying that the carbon species were not incorporated into the lattice of the TiO$_2$. Moreover, the graphene–TiO$_2$ composites extend their broad background absorption into the visible-light region, due to the presence of graphene in the graphene–TiO$_2$ composites.[21] In contrast to the
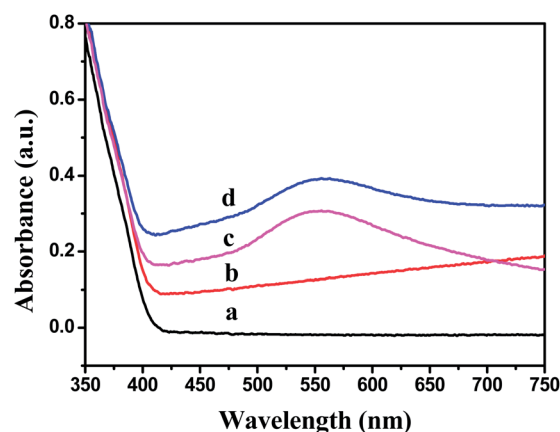

Fig. 4 UV-vis diffuse reflectance spectra of the P (a), PG (b), PA25 (c) and PGA25 (d) samples.

4 | J. Mater. Chem. A, 2014, xx, 1–10

This journal is © The Royal Society of Chemistry 2014

pure TiO_2 and graphene–TiO_2 composites (samples P and PG), the samples deposited with Au NPs (samples PA25 and PGA25) have a significantly enhanced light absorption in the visible region, with a broad band peak located at around 550 nm, arising from the SPR effect of the gold nanoparticles.[31,32]

3.4. Raman spectra

Raman scattering spectroscopy can provide valuable information on the phase composition, crystallinity, crystallite size, and defect (oxygen vacancy) concentrations of TiO_2. Moreover, it can also characterize the crystalline quality of carbon and reflect the structural changes from GO to graphene. Fig. 5 shows a comparison of the Raman spectra of GO, graphene–TiO_2 (PG), the Au–TiO_2 composite (PA25) and the Au–TiO_2–graphene composite (PGA25). For the PG, PA25 and PGA25 samples (Fig. 5b–d), there are several characteristic bands at 395, 517, 636 and 446 cm^{-1} corresponding to the $B_{1g(1)}$, $A_{1g} + B_{1g(2)}$, and $E_{g(2)}$ modes of anatase and the E_g mode of rutile, respectively.[9,33,34] Two typical Raman bands can be observed in Fig. 5a for the sample GO. One band at around 1363 cm^{-1} (called the D-band) relates to the occurrence of defects and structural disorder in graphene. The other band, at around 1596 cm^{-1} (G-band), is due to the stretching of the sp^2-hybridized carbon–carbon bonds.[35] For the PG and PGA25 samples, the two characteristic peaks at about 1345 or 1340 cm^{-1} (D band) and 1604 or 1597 cm^{-1} (G band) for the graphitized structures can be found in Fig. 5b and d. In addition, the D/G intensity ratios for the samples PG and PGA25 are higher than that of pure GO, which indicates the reduction of the exfoliated GO and confirms the existence of graphene sheets in the graphene–TiO_2 composite.[21,36]

A further observation indicates that the Raman scattering bands of the samples PA25 and PGA25 are enhanced with incorporation of Au particles. Moreover, the Raman scattering intensity of the PGA25 sample is much higher than that of the PA25 sample. This is ascribed to the surface enhanced Raman scattering (SERS) effect from the Au particles, in which the interplay 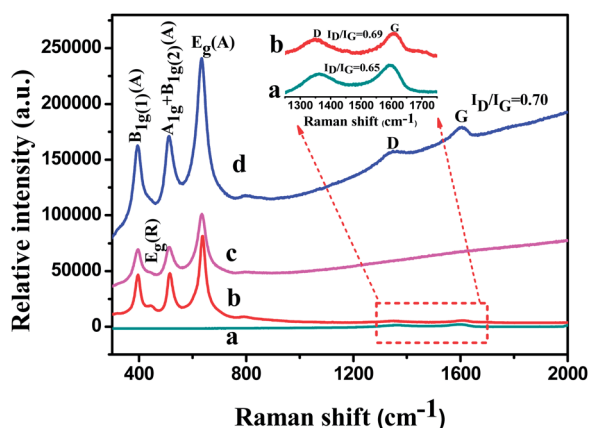between the Au NPs and the molecules/ions adsorbed on the surface of the Au NPs incurs the SERS.[37] Considering the intimate contact and good incorporation among the Au, TiO_2 and graphene in the PGA25 sample (Fig. 2), the interaction in the Au–graphene and Au–TiO_2 may also contribute to the observed SERS effect in the PGA25 sample.[37–39] It is now generally accepted that there are two interacting mechanisms which explain the overall SERS effect. One is the electromagnetic (EM) mechanism, in which a strong concentrated local electric field enhances the Raman scattering efficiency, through the electromagnetic coupling between the molecules and the metal surface.[37,40] The other is the chemical mechanism, in which the photoinduced metal-molecule charge transfer (CT) is believed to be responsible for the chemical enhancement in the SERS.[41] Generally, the two mechanisms simultaneously occur on the Raman enhancement.[41,42] In this study, the incident laser wavelength ($\lambda = 514.5$ nm) coincided with the absorptive band of the Au–TiO_2–graphene system (Fig. 4). When the Au–TiO_2–graphene composite sample was irradiated by a laser at $\lambda = 514.5$ nm, the surface plasmon modes of the Au NPs on the composite samples were excited, producing a strong local electromagnetic field around the gold NPs. At the same time, the charge-transfer interaction between the Au NPs and the graphene–TiO_2 composite rendered a short-range chemical effect, resulting in an enhancement of the SERS. Moreover, the existence of graphene, which works as an excellent electron transmission unit, increases the feasibility of the charge-transfer between the gold NPs, graphene and TiO_2.[37] Combining these effects, the intensity of the Raman bands assigned to the Raman-active vibration modes of TiO_2 and graphene are evidently enhanced; whereas under the same conditions, the pure GO and graphene–TiO_2 composite samples show a relatively weak Raman scattering. This result not only displays the enhanced Raman scattering for the Au–TiO_2–graphene plasmonic nanostructure, but also shows the strong interaction among the Au NPs, graphene and TiO_2 in the Au–TiO_2–graphene system.

3.5. XPS analysis

To investigate the reduction degree of GO and the state of the Au species in the microwave-assisted hydrothermal reduction process, the high-resolution XPS spectra of C1s, for the GO and PGA25 samples, and Au 4f for the PGA25 sample were collected (Fig. 6). In the deconvoluted C1s spectra of GO (Fig. 6a), the peak centered at 284.8 eV is ascribed to adventitious carbon and sp^2 hybridized carbon (C–C), while the peaks at higher binding energies are attributed to oxygen-containing species, such as epoxy/hydroxyls (C–O, 287.0 eV), and carboxyl (O–C=O, 288.9 eV).[19,43] In comparison, in the C1s XPS spectrum of the PGA25 sample (Fig. 6b), the peaks for C–O and O–C=O remarkably decrease, indicating the efficient removal of the oxygen-containing functional groups from the GO. Furthermore, the reduction degree of the GO can be quantified by the relative content of oxygen-bound carbon, which is calculated using eqn (2):[44]

$$\%O\text{-bound C} = \frac{A_{C-O} + A_{O-C=O}}{A_{C-C} + A_{C-O} + A_{O-C=O}} \times 100\% \quad (2)$$

Fig. 5 Raman spectra of the GO (a), PG (b), PA25 (c) and PGA25 (d) samples.

This journal is © The Royal Society of Chemistry 2014

J. Mater. Chem. A, 2014, xx, 1–10 | 5
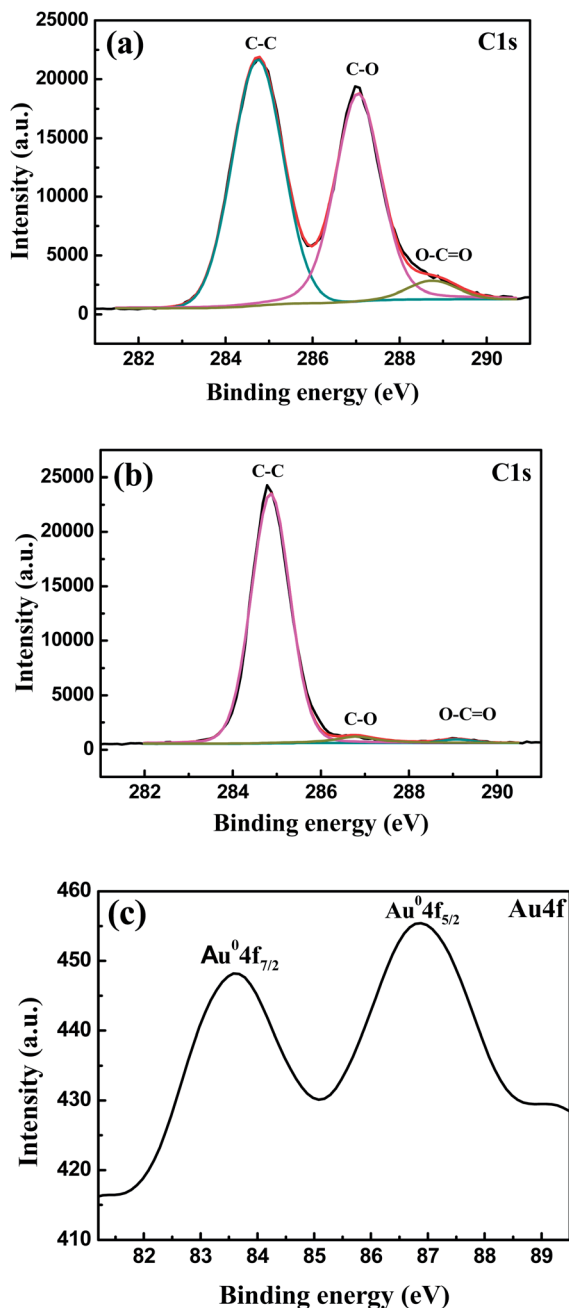
Fig. 6 High-resolution XPS spectra of C 1s for the GO (a) and PGA25 (b) samples and Au 4f for the PGA25 (c) sample.

of the Au species are located at respectively, 83.6 and 86.8 eV, suggesting that the Au species in the Au–graphene–TiO$_2$ composites is in the metallic state.[45–47] Compared with the generally accepted binding energies of 4f$_{7/2}$ (84.0 eV) and 4f$_{5/2}$ (87.7 eV) for metallic Au, the variations in the binding energies are ascribed to the change of their Fermi levels, after the combination of Au with TiO$_2$ and graphene, which demonstrates the strong interactions between them.[45–47] This XPS result is in good agreement with the result obtained by Raman scattering spectroscopy.

3.6. Photocatalytic H$_2$-production activity

The H$_2$-production activity on various samples was evaluated under 420 nm-LED irradiation, using methanol as the scavenger. Fig. 7 and Table 1 present the comparison of the photocatalytic H$_2$ production activity of the TiO$_2$ (P), graphene–TiO$_2$ (PG), Au–TiO$_2$ (PA25), and Au–TiO$_2$–graphene samples (samples PGA05 to PGA50). No appreciable H$_2$ production was detected in the absence of either irradiation or the photocatalyst, indicating that hydrogen was produced by photocatalytic reactions on the photocatalyst. As can be seen from this figure, the Au content has a significant influence on the photocatalytic activity of TiO$_2$. For pure TiO$_2$, it shows no appreciable H$_2$ production, which can be ascribed to the following factors: (1) the energy and intensity of the 420 nm LED light is not enough to excite it; (2) the rapid recombination between the CB electrons and VB holes in the pure TiO$_2$; and (3) the presence of a large H$_2$-evolution overpotential on the TiO$_2$ surface. Furthermore, after the incorporation of a small amount of graphene, H$_2$ production is not observed. This indicates that the graphene can not be excited by visible light to produce photoelectrons. In this case, the graphene only works as the reservoir and transmission unit for the electrons, rather than as the electron-production site for H$_2$ production.

Nevertheless, after the introduction of the Au NPs, the hydrogen evolution rate becomes higher as the Au

where $A_{C–C}$, $A_{C–O}$ and $A_{O–C=O}$ are the peak areas for graphitic carbon (C–C), and oxidized carbon (C–O, O–C=O), respectively. According to the calculation, the as-obtained GO has 52% oxidized carbon and 48% graphitic carbon, while 7% oxidized carbon and 93% graphitic carbon occur for the PGA25 sample, showing that vast majority of the oxygen-containing functional groups were removed from the GO, with the formation of graphene, during the microwave-assisted hydrothermal reduction process.

The high-resolution XPS spectra also confirm the existence of Au in the PGA25 sample (Fig. 6c). The peaks of 4f$_{7/2}$ and 4f$_{5/2}$
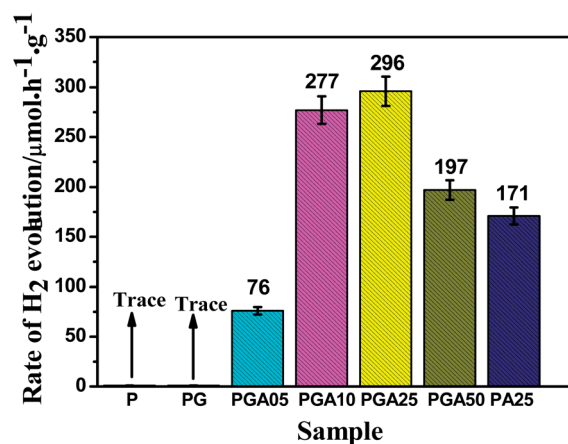

Fig. 7 Comparison of photocatalytic activity of the P, PG, PGA05, PGA10, PGA25, PGA50 and PA25 samples for the photocatalytic H$_2$ production from methanol aqueous solution under 420 nm-LED light irradiation.

6 | J. Mater. Chem. A, 2014, xx, 1–10

This journal is © The Royal Society of Chemistry 2014

concentration increases up to 0.25%. This means that the gold NPs play an important role in the visible-light-induced photo-catalytic activities. The higher content of gold nanoparticles leads to more light absorption *via* SPR, and thereby a higher photocatalytic activity. However, excess Au NPs in the nano-composites could act as a recombination center of the photo-generated charges and then reduce the photocatalytic activity, which is evidenced by the lower H_2 evolution rate for the PGA50 sample, compared to the PGA25 sample.[46] For the PA25 sample, the H_2-production rate decreased to 171 μmol h^{-1} g^{-1} with a 2.4% QE, which is nearly half of the PGA25 sample (296 μmol h^{-1} g^{-1}, 4.1% QE), indicating that the presence of graphene, functioning as an electron reservoir to transfer and separate electrons and holes, is greatly favorable to the H_2 production.

The high H_2-production activity of the PGA25 sample under visible-light irradiation can be understood, as illustrated in Fig. 8a. At first, the Au NPs are photo-excited under 420 nm light irradiation, due to plasmonic resonance, and charge separation is accomplished by the transfer of photo-excited electrons from the Au nanoparticles to the TiO_2 conduction band. Meanwhile, the CB electrons of TiO_2 tend to transfer into the graphene sheets in a graphene–TiO_2 system, because the graphene/graphene$^-$ redox potential (−0.08 eV) is slightly lower than the CB of TiO_2 (−0.24 eV).[21,48] The mobility of these electrons on the
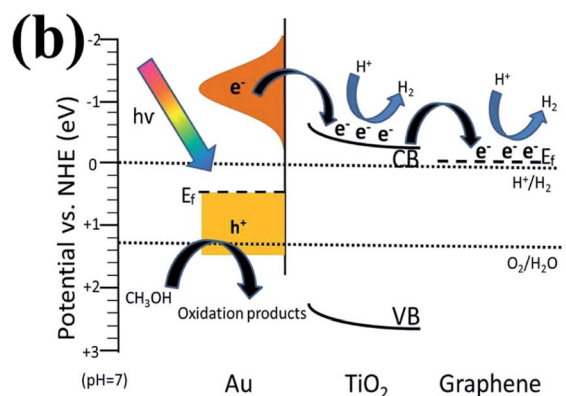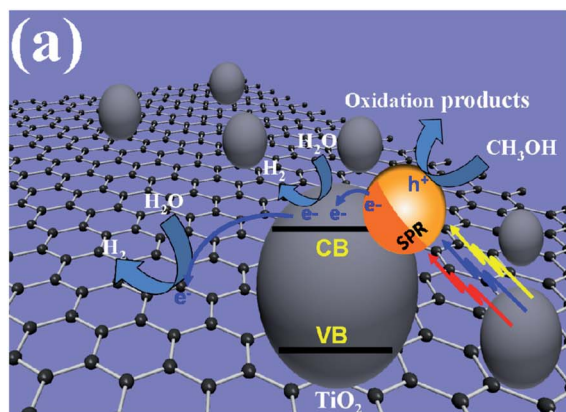

Fig. 8 Schematic diagram (a) and proposed mechanism (b) illustrating the energy band structure, and electron–hole pair transfer and separation in the Au–TiO_2–graphene composite for photocatalytic H_2-production under visible light irradiation.

graphene sheets is high. Thus, both the graphene surface and the CB of TiO_2 can function as active sites for H_2 production, simultaneously. Such a scenario retards the recombination of the photogenerated electron–hole pairs and suppresses the reverse reaction by separating the evolution sites of hydrogen and oxygen. Thereby, the PGA25 sample has a better H_2-production activity than the PA25 sample. The detailed mechanism of H_2-production activity of the PGA25 sample under visible-light irradiation can be explained as in Fig. 8b. The Fermi level for Au is around 0.6 eV (work function, ∼5.1 eV),[49] lower than the conduction band of the TiO_2.[21] After they make contact with each other, there is a ∼1.0 eV Schottky barrier at the interface between the gold and TiO_2,[50] which will hinder electrons transferring from the Au NPs to the TiO_2. However, the electron injection from Au NPs to TiO_2 on SPR excitation has been proven to be feasible.[50,51] One possible mechanism suggested that, under visible-light irradiation, the Au NPs would give rise to the SPR effect. Electrons oscillating collectively on the SPR excitation may lead to an interband excitation, generating some energetic electrons, of which the energy is above 1.0 eV, with respect to the Au Fermi level. Also, the energetic electrons generated in the process of the SPR excitation would overcome the Schottky barrier and transfer electrons to the CB of the TiO_2. At the moment, some energetic electrons reduce H^+ to H_2, and another energetic electrons in the CB of TiO_2 can be further transferred to the graphene sheets, to produce H_2, due to the fact that the potential of graphene/graphene$^-$ is lower than the CB of TiO_2 and slightly higher than the potential of H^+/H_2 (0 V). Moreover, the excitation of SPR can result in the generation of plasmonic near-fields in the Au–TiO_2 interface. Thus, the localized electronic states in the band gap of the TiO_2 can be excited and electrons can be transferred to the CB of the TiO_2,[15] and further moved to the graphene sheet, to produce H_2. Consequently, the Au–TiO_2–graphene sample shows an enhanced photocatalytic H_2-production activity, compared to the pure TiO_2, graphene–TiO_2 and Au–TiO_2 samples. It should be noted that no H_2-production activity was observed for the prepared graphene–Au composite (GA) sample, indicating the important role of TiO_2 for the studied system. The detailed mechanism needs to be further investigated.

3.7. Transient photocurrent response and EIS analysis

To provide additional evidence for the above suggested photo-catalytic water splitting mechanism, the transient photocurrent responses of the P, PG, PA25 and PGA25 sample electrodes were recorded for several on–off cycles, under intermittent 420 nm LED-light irradiation, at a bias potential of 0.5 V. As shown in Fig. 9, an apparently boosted photocurrent response appears for all the samples under visible light illumination, and the on–off cycles of the photocurrent are highly reproducible. This indicates that most of the photoelectrons are transferred to the cathode, across the sample, to produce a photocurrent under visible light irradiation.[52] Conspicuously, the photocurrent curves of all the samples display the same shape, including an anodic photocurrent spike at the initial irradiation. The initial anodic photocurrent spike results from the separation of the
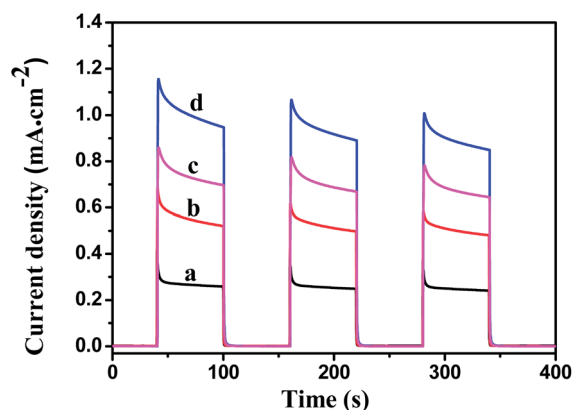
Fig. 9 The transient photocurrent responses of the P (a), PG (b), PA25 (c) and PGA25 (d) samples in a 0.5 M Na_2SO_4 aqueous solution under 420 nm-LED light irradiation at 0.5 V *vs.* Ag/AgCl.
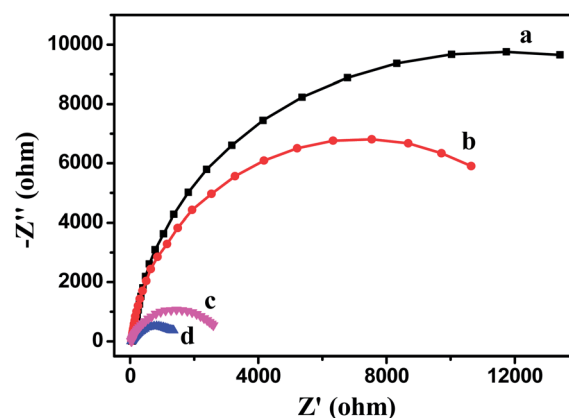

Fig. 10 Nyquist plots of the P (a), PG (b), PA25 (c) and PGA25 (d) sample electrodes in 0.5 M Na_2SO_4 aqueous solution under 420 nm-LED light irradiation.

photoelectron and hole within the photo-electrode. Photo-induced holes are then transferred to the sample surface and trapped or captured by a reduced species in the electrolyte, while the photo-induced electrons are transported to the cathode, *via* TiO_2 or graphene.[21,53] After the spike current has been attained, there is a continuous decrease in the photocurrent, before reaching a constant current. This indicates that the holes accumulated at the sample surface competitively recombine with electrons from the Au nanoparticles, instead of being trapped, or captured by a reduced species in the electrolyte. Notably, the highest transient photocurrent was obtained for the PGA25 sample, compared with the P, PG and PA25 samples. Firstly, the Au present can absorb visible light and generate more photoelectrons due to the SPR effect. Moreover, the formation of a Schottky junction at the Au–TiO_2 interface can separate the photoelectrons and holes, and thus increase the photocurrent. Secondly, graphene is an excellent electron-acceptor, with a superior conductivity, due to its two-dimensional π-conjugation structure,[54] which can act as an electron collector and transporter in the PGA25 samples. That effectively suppresses the charge recombination, leaving more charge carriers to form reactive species. Therefore, the highest photocurrent response and photocatalytic H_2-production rate were obtained over the PGA25 sample.

Electrochemical impedance spectra (EIS) analysis is useful in studying the charge transfer process occurring in a three-electrode system. Fig. 10 displays the EIS Nyquist plots of the P, PG, PA25 and PGA25 samples. The observed semicircles correspond to the charge transfer resistance at the sample–electrode interface. The smaller the semicircle arc is, the easier the charge transfer is.[9,55] As can be seen from Fig. 10, the PGA25 sample shows the smallest semicircle in the middle-frequency region, in comparison to the P, PG and PA25 samples, which indicates the fastest interfacial electron transfer. The existence of a Schottky junction at the interface of Au–TiO_2 is in favor of the separation of photoelectrons and holes. Moreover, because of the excellent conductivity, the introduction of graphene, which functions as an electron collector and transporter, can

benefit the charge transfer in the PGA25 sample and inhibit the charge recombination. Thus, the photocatalytic H_2-production activity of the PGA25 sample can be significantly enhanced.

4. Conclusions

In conclusion, a simple, one-step microwave-assisted hydrothermal method was successfully developed to synthesize highly active graphene based Au–TiO_2 photocatalysts, with a visible light response for photocatalytic H_2 production. Owing to the fact that the surface plasmon resonance effect of the Au NPs broadens the visible light response of the TiO_2, and the excellent electron transport properties of graphene hinders the fast recombination of photoelectron and hole pairs, such composite photocatalysts showed a significantly increased visible light absorption and enhanced photocatalytic H_2-production activity, than the pure TiO_2, graphene–TiO_2 and Au–TiO_2 composites. The photocurrent response and EIS experiments further demonstrated the suggested mechanism. This work exhibits a new visible light response photocatalyst, fabricated by a facile microwave-assisted hydrothermal method, in the application of hydrogen production, which will provide new insights into the design and fabrication of novel, visible-light driven photocatalytic materials.

Acknowledgements

Notes and references

1 K. Shimura and H. Yoshida, *Energy Environ. Sci.*, 2011, **4**, 2467.

2 (*a*) Y. Q. Wu, G. X. Lu and S. B. Li, *J. Phys. Chem. C*, 2009, **113**, 9950; (*b*) Q. J. Xiang and J. G. Yu, *J. Phys. Chem. Lett.*, 2013, **4**, 753; (*c*) P. Gao, Z. Y. Liu and D. D. Sun, *J. Mater. Chem. A*, 2013, **1**, 14262; (*d*) J. Jin, J. Yu, G. Liu and P. K. Wong, *J. Mater. Chem. A*, 2013, **1**, 10927.

3 (*a*) K. Fuku, T. Kamegawa, K. Mori and H. Yamashita, *Chem.–Asian J.*, 2012, **7**, 1366; (*b*) C. Z. Wen, J. Z. Zhou, H. B. Jiang, Q. H. Hu, S. Z. Qiao and H. G. Yang, *Chem. Commun.*, 2011, **47**, 4400; (*c*) J. Yu, Y. Wang and W. Xiao, *J. Mater. Chem. A*, 2013, **1**, 10727.

4 (*a*) A. Mitsionis, T. Vaimakis, C. Trapalis, N. Todorova, D. Bahnemann and R. Dillert, *Appl. Catal., B*, 2011, **106**, 398; (*b*) J. G. Yu, Y. Hai and B. Cheng, *J. Phys. Chem. C*, 2011, **115**, 4953.

5 A. Tanaka, S. Sakaguchi, K. Hashimoto and H. Kominami, *ACS Catal.*, 2013, **3**, 79.

6 R. Dholam, N. Patel, M. Adami and A. Miotello, *Int. J. Hydrogen Energy*, 2009, **34**, 5337.

7 Q. Xiao and L. Gao, *J. Alloys Compd.*, 2013, **551**, 286.

8 V. J. Babu, M. K. Kumar, A. S. Nair, T. L. Kheng, S. I. Allakhverdiev and S. Ramakrishna, *Int. J. Hydrogen Energy*, 2012, **37**, 8897.

9 J. G. Yu, J. J. Fan and B. Cheng, *J. Power Sources*, 2011, **196**, 7891.

10 A. Galinska and J. Walendziewski, *Energy Fuels*, 2005, **19**, 1143.

11 B. Zielinska, E. Borowiak-Palen and R. J. Kalenczuk, *Int. J. Hydrogen Energy*, 2008, **33**, 1797.

12 L. F. Qi, J. G. Yu and M. Jaroniec, *Phys. Chem. Chem. Phys.*, 2011, **13**, 8915.

13 S. Sakthivel, M. V. Shankar, M. Palanichamy, B. Arabindoo, D. W. Bahnemann and V. Murugesan, *Water Res.*, 2004, **38**, 3001.

14 (*a*) X. Zhou, G. Liu, J. Yu and W. Fan, *J. Mater. Chem.*, 2012, **22**, 21337; (*b*) K. Kimura, S. Nara, Y. Jin-nouchi and H. Tada, *J. Phys. Chem. C*, 2012, **116**, 7111.

15 Z. W. Seh, S. H. Liu, M. Low, S. Y. Zhang, Z. L. Liu, A. Mlayah and M. Y. Han, *Adv. Mater.*, 2012, **24**, 2310.

16 D. H. Zhang, G. D. Li, J. X. Li and J. S. Chen, *Chem. Commun.*, 2008, **29**, 3414.

17 G. H. Chan, J. Zhao, E. M. Hicks, G. C. Schatz and R. P. Van Duyne, *Nano Lett.*, 2007, **7**, 1947.

18 (*a*) Q. J. Xiang, J. G. Yu and M. Jaroniec, *J. Am. Chem. Soc.*, 2012, **134**, 6575; (*b*) Q. J. Xiang, J. G. Yu and M. Jaroniec, *Chem. Soc. Rev.*, 2012, **41**, 782.

19 (*a*) Q. Li, B. D. Guo, J. G. Yu, J. R. Ran, B. H. Zhang, H. J. Yan and J. R. Gong, *J. Am. Chem. Soc.*, 2011, **133**, 10878; (*b*) P. H. Wang, Y. X. Tang, Z. L. Dong, Z. Chen and T. T. Lim, *J. Mater. Chem. A*, 2013, **1**, 4718; (*c*) J. X. Low, J. G. Yu, Q. Li and B. Cheng, *Phys. Chem. Chem. Phys.*, 2014, **16**, 1111.

20 I. V. Lightcap, T. H. Kosel and P. V. Kamat, *Nano Lett.*, 2010, **10**, 577.

21 Q. J. Xiang, J. G. Yu and M. Jaroniec, *Nanoscale*, 2011, **3**, 3670.

22 Y. X. Xu, H. Bai, G. W. Lu, C. Li and G. Q. Shi, *J. Am. Chem. Soc.*, 2008, **130**, 5856.

23 K. S. W. Sing, D. H. Everett, R. A. W. Haul, L. Moscou, R. A. Pierotti, J. Rouquerol and T. Siemieniewska, *Pure Appl. Chem.*, 1985, **57**, 603.

24 S. Zhu, S. Liang, Q. Gu, L. Xie, J. Wang, Z. Ding and P. Liu, *Appl. Catal., B*, 2012, **119–120**, 146.

25 Y. Fan, X. Yang, C. P. Yang and J. H. Liu, *Electroanalysis*, 2012, **24**, 1334.

26 J. G. Yu, Y. R. Su and B. Cheng, *Adv. Funct. Mater.*, 2007, **17**, 1984.

27 J. G. Yu and J. R. Ran, *Energy Environ. Sci.*, 2011, **4**, 1364.

28 S. W. Liu, J. G. Yu and M. Jaroniec, *J. Am. Chem. Soc.*, 2010, **132**, 11914.

29 W. G. Wang, J. G. Yu, Q. J. Xiang and B. Cheng, *Appl. Catal., B*, 2012, **119–120**, 109.

30 H. Yu, H. Irie and K. Hashimoto, *J. Am. Chem. Soc.*, 2010, **132**, 6898.

31 D. Tsukamoto, Y. Shiraishi, Y. Sugano, S. Ichikawa, S. Tanaka and T. Hirai, *J. Am. Chem. Soc.*, 2012, **134**, 6309.

32 Z. H. Zhang, L. B. Zhang, M. N. Hedhili, H. N. Zhang and P. Wang, *Nano Lett.*, 2013, **13**(1), 14.

33 (*a*) J. G. Yu, T. T. Ma and S. W. Liu, *Phys. Chem. Chem. Phys.*, 2011, **13**, 3491; (*b*) J. G. Yu, T. T. Ma, G. Liu and B. Cheng, *Dalton Trans.*, 2011, **40**, 6635.

34 J. Zhang, M. J. Li, Z. C. Feng, J. Chen and C. Li, *J. Phys. Chem. B*, 2006, **110**, 927.

35 Y. Y. Wen, H. M. Ding and Y. K. Shan, *Nanoscale*, 2011, **3**, 4411.

36 S. Stankovich, D. A. Dikin, R. D. Piner, K. A. Kohlhaas, A. Kleinhammes, Y. Jia, Y. Wu, S. T. Nguyen and R. S. Ruoff, *Carbon*, 2007, **45**, 1558.

37 X. Jiang, X. L. Li, X. F. Jia, G. Z. Li, X. Wang, G. Y. Wang, Z. S. Li, L. B. Yang and B. Zhao, *J. Phys. Chem. C*, 2012, **116**, 14650.

38 X. Ling, J. X. Wu, L. M. Xie and J. Zhang, *J. Phys. Chem. C*, 2013, **117**, 2369.

39 L. B. Gao, W. C. Ren, B. L. Liu, R. Saito, Z. S. Wu, S. S. Li, C. B. Jiang, F. Li and H. M. Cheng, *ACS Nano*, 2009, **3**, 933.

40 Q. J. Xiang, J. G. Yu, B. Cheng and H. C. Ong, *Chem. – Asian J.*, 2010, **5**, 1466.

41 H. Xu, L. M. Xie, H. L. Zhang and J. Zhang, *ACS Nano*, 2011, **5**, 5338.

42 Y. K. Yang, C. E. He, W. J. He, L. J. Yu, R. G. Peng, X. L. Xie, X. B. Wang and Y. W. Mai, *J. Nanopart. Res.*, 2011, **13**, 5571.

43 S. Stankovich, R. D. Piner, X. Q. Chen, N. Q. Wu, S. T. Nguyen and R. S. Ruoff, *J. Mater. Chem.*, 2006, **16**, 155.

44 A. Iwase, Y. H. Ng, Y. Ishiguro, A. Kudo and R. Amal, *J. Am. Chem. Soc.*, 2011, **133**, 11054.

45 Y. M. Wu, H. B. Liu, J. L. Zhang and F. Chen, *J. Phys. Chem. C*, 2009, **113**, 14689.

46 J. Fang, S. W. Cao, Z. Wang, M. M. Shahjamal, S. C. J. Loo, J. Barber and C. Xue, *Int. J. Hydrogen Energy*, 2012, **37**, 17853.

47 Z. H. Xu, J. G. Yu and G. Liu, *Electrochem. Commun.*, 2011, **13**, 1260.

48 X. Wang, L. J. Zhi and K. Mullen, *Nano Lett.*, 2008, **8**, 323.

This journal is © The Royal Society of Chemistry 2014

J. Mater. Chem. A, 2014, **xx**, 1–10 | 9

49 R. N., M. Deepa and A. K. Srivastava, *Phys. Chem. Chem. Phys.*, 2012, **14**, 767.

50 A. Furube, L. Du, K. Hara, R. Katoh and M. Tachiya, *J. Am. Chem. Soc.*, 2007, **129**, 14852.

51 Y. Tian and T. Tatsuma, *J. Am. Chem. Soc.*, 2005, **127**, 7632.

52 A. Hagfeldt, H. Lindstrom, S. Sodergren and S. Lindquist, *J. Electroanal. Chem.*, 1995, **381**, 39.

53 G. P. Dai, J. G. Yu and G. Liu, *J. Phys. Chem. C*, 2011, **115**, 7339.

54 K. S. Novoselov, A. K. Geim, S. V. Morozov, D. Jiang, Y. Zhang, S. V. Dubonos, I. V. Grigorieva and A. A. Firsov, *Nature*, 2005, **438**, 197.

55 A. Jana, C. Bhattacharya and J. Datta, *Electrochim. Acta*, 2010, **55**, 6553.